THE ASTROPHYSICAL JOURNAL, 443:329–340, 1995 April 10

A REANALYSIS OF THE SWP-HI *IUE* OBSERVATIONS OF CAPELLA

BRIAN E. WOOD[1] AND THOMAS R. AYRES[2]
Received 1994 June 27; accepted 1994 October 19

ABSTRACT

We have reanalyzed the numerous high-resolution, far-ultraviolet observations of Capella (G8 III + G1 III) made by the *International Ultraviolet Explorer* in its 16 yr lifetime. Our purpose was to search for long-term profile variations in Capella's ultraviolet emission lines and to complement the analysis of Goddard High Resolution Spectrograph (GHRS) observations of Capella, discussed in a companion paper (Linsky et al. 1995). We implemented a state-of-the-art photometric correction and spectral extraction procedure to improve S/N and control potential sources of systematic errors. Nevertheless, we were unable to find compelling evidence for any significant long-term line profile variations.

Previous work has shown that the G8 primary star is only a minor contributor to the high-excitation transition region lines but is a significant contributor to the low-excitation chromospheric lines. We have found exceptions to this rule, however. We find that the G8 star is responsible for a significant portion of Capella's N V λλ1239, 1243 emission, but is not a large contributor to the S I λ1296, Cl I λ1352, and O I] λ1356 lines. We suggest possible explanations for these behaviors. We also find evidence that the He II λ1640 emission from the G1 star is from the transition region, while the He II λ1640 emission from the G8 star is chromospheric, consistent with the findings of Linsky et al. (1994).

The C II λ1336 line shows a weak central reversal. It is blueshifted by about 9 km s^{-1} with respect to the centroid of the emission from the G1 star. While the central reversal of the C II line is blueshifted, the central reversal of the Si III λ1207 line discussed by Linsky et al. (1994) is not.

Subject headings: binaries: close — stars: individual (α Aurigae) — stars: late-type — ultraviolet: stars

1. INTRODUCTION

Capella (G8 III + G1 III) is a well-known spectroscopic binary system with an orbital period of 104 days. The physical parameters of the Capella stars are discussed in detail by Hummel et al. (1994) and by Batten, Hill, & Lu (1991). The G8 primary is slightly more massive than the G1 secondary (2.69 $M_\odot$ and 2.56 $M_\odot$, respectively). Capella has been a popular target for spectroscopic studies in the ultraviolet (e.g., Dupree 1975; Ayres & Linsky 1980; Ayres 1984, 1988), extreme ultraviolet (e.g., Dupree et al. 1993), and X-rays (e.g., Lemen et al. 1989). Capella is a prominent source at all of these wavelengths owing to high intrinsic brightness and close proximity (d = 13.3 pc).

Ayres & Linsky (1980) used data taken by the *International Ultraviolet Explorer* (*IUE*) to show that the G1 star is the dominant contributor to the emission lines in Capella's strong UV emission line spectrum. In general, the G1 star is more dominant in high excitation transition region lines such as C IV λ1548 than it is in low excitation chromospheric lines such as Mg II λ2796. Since the G1 star rotates much faster than the G8 star (v sin i = 36 km s^{-1} compared with v sin i = 3 km s^{-1}; Strassmeier & Fekel 1990), the Capella system nicely illustrates the connection between rotation and stellar activity that has been the subject of considerable study in many wavelength regions (e.g., Skumanich 1972; Pallavicini et al. 1981; Wood et al. 1994). Further analyses of *IUE* observations have revealed that Capella's UV line fluxes are surprisingly constant with time, and that many of Capella's UV emission lines are significantly redshifted, with the high-excitation transition region lines generally having the larger redshifts (Ayres 1984, 1988). The line redshifts have been interpreted as being due to mass flows in the chromosphere and transition region of the Capella secondary.

More recently, a series of observations of Capella was made with the Goddard High Resolution Spectrograph (GHRS) aboard the *Hubble Space Telescope* (*HST*) (Linsky et al. 1995, hereafter Paper II). These observations utilized the low-, medium-, and high-resolution gratings. The emission-line profiles produced by relatively short integrations with the GHRS medium- and high-resolution gratings are superior in quality to those produced by typical single exposures with the *IUE* SWP echelle. Nevertheless, the extensive set of *IUE* observations of Capella still has considerable value, particularly because many important spectral features could not be observed at all with the GHRS, given its limited spectral coverage. Furthermore, with the exception of Lyman-α and Mg II λλ2796, 2803, none of the features was observed by the GHRS at more than one orbital phase, making it difficult to determine the relative contributions of the G8 and G1 stars to each line.

Ayres et al. (1993, hereafter Paper I) reanalyzed *IUE* observations of H I Lyα to complement the analysis of the GHRS echelle observations of that line (Linsky et al. 1993). Although Capella's UV emission line fluxes in general are quite stable, Paper I found significant long-term profile variations in the Lyα line. One goal of our present work is to use the extensive set of *IUE* SWP-HI observations of Capella to search for profile variations in other UV emission lines. In Paper II, Linsky et al. have used the full set of GHRS observations of Capella to determine the properties of the chromospheres and transition regions of the Capella stars. The present paper, a companion to Paper II, attempts to confirm and extend the findings of that study using the full *IUE* data set, including the

[1] Joint Institute for Laboratory Astrophysics, University of Colorado, Boulder, CO 80309-0440; wood@jila.colorado.edu.
[2] Center for Astrophysics and Space Astronomy, University of Colorado, Boulder, CO 80309-0391; ayres@vulcan.colorado.edu.

TABLE 1

LARGE-APERTURE *IUE* OBSERVATIONS OF CAPELLA

ID Number	SWP Number	Exposure Time (minutes)	J.D. 2,443,000+	Orbital Phase	Observer	ID Number	SWP Number	Exposure Time (minutes)	J.D. 2,443,000+	Orbital Phase	Observer
1	7104	19.0	1184.0	0.10	Black	54	13756	60.0	1714.5	0.20	Ayres
2	8178	30.0	1305.4	0.27	Ayres	55	13757	10.0	1714.5	0.20	Ayres
3	8181	30.0	1305.5	0.27	Ayres	56	13773	60.0	1716.4	0.22	Ayres
4	8182	30.0	1305.6	0.27	Ayres	57	13774	10.0	1716.4	0.22	Ayres
5	8183	30.0	1305.6	0.27	Ayres	58	13791	60.0	1718.5	0.24	Ayres
6	8626	10.0	1331.3	0.52	Schiffer	59	13792	10.0	1718.6	0.24	Ayres
7	8627	30.0	1331.4	0.52	Schiffer	60	13808	30.0	1720.5	0.26	Ayres
8	8628	25.0	1331.4	0.52	Schiffer	61	13821	10.0	1722.4	0.27	Baroff
9	8629	25.0	1331.4	0.52	Schiffer	62	13823	25.0	1722.5	0.28	Baroff
10	8630	25.0	1331.5	0.52	Schiffer	63	13825	60.0	1722.5	0.28	Baroff
11	8631	25.0	1331.5	0.52	Schiffer	64	13842	40.0	1724.3	0.29	Ayres
12	8632	10.0	1331.6	0.52	Schiffer	65	13843	10.0	1724.3	0.29	Ayres
13	8832	30.0	1356.3	0.76	Schiffer	66	18779	15.0	2315.8	0.98	Ayres
14	8833	30.0	1356.3	0.76	Schiffer	67	18781	80.0	2315.9	0.98	Ayres
15	8834	30.0	1356.4	0.76	Schiffer	68	18786	22.5	2316.8	0.99	Ayres
16	8835	30.0	1356.4	0.76	Schiffer	69	18788	97.0	2316.9	0.99	Ayres
17	8836	30.0	1356.5	0.76	Schiffer	70	18792	22.5	2317.8	0.00	Ayres
18	8837	30.0	1356.5	0.76	Schiffer	71	18794	137.0	2317.9	0.00	Ayres
19	8838	30.0	1356.6	0.76	Schiffer	72	18799	22.5	2318.8	0.01	Ayres
20	11028	60.0	1616.6	0.26	Simon	73	18801	108.0	2318.9	0.01	Ayres
21	11030	10.0	1616.6	0.26	Simon	74	18803	22.5	2319.8	0.02	Ayres
22	11032	60.0	1616.7	0.26	Simon	75	18805	106.0	2319.9	0.02	Ayres
23	11033	60.0	1616.7	0.26	Simon	76	18810	22.5	2320.8	0.03	Ayres
24	13446	60.0	1673.4	0.80	Seab	77	18812	148.0	2320.9	0.03	Ayres
25	13447	10.0	1673.4	0.80	Seab	78	21200	15.0	2608.0	0.79	Ayres
26	13468	60.0	1676.4	0.83	Brugel	79	21201	60.0	2608.1	0.79	Ayres
27	13469	10.0	1676.4	0.83	Brugel	80	27119	90.0	3385.4	0.26	Ayres
28	13488	60.0	1678.4	0.85	Brugel	81	27120	90.0	3385.5	0.26	Ayres
29	13489	12.0	1678.4	0.85	Brugel	82	27124	15.0	3385.9	0.27	Ayres
30	13535	60.0	1683.4	0.90	Mullan	83	27445	90.0	3435.2	0.74	Ayres
31	13536	10.0	1683.5	0.90	Mullan	84	27446	90.0	3435.3	0.74	Ayres
32	13558	10.0	1687.4	0.94	Ayres	85	27452	15.0	3435.7	0.75	Ayres
33	13560	25.0	1687.5	0.94	Ayres	86	28058	35.0	3520.3	0.56	Ayres
34	13578	50.0	1689.5	0.96	Simon	87	28063	35.0	3520.5	0.56	Ayres
35	13579	10.0	1689.5	0.96	Simon	88	28064	35.0	3520.6	0.56	Ayres
36	13597	50.0	1691.5	0.98	Simon	89	34713	2×100.0	4475.4	0.74	Ayres
37	13598	10.0	1691.6	0.98	Simon	90	34714	2×100.0	4475.6	0.74	Ayres
38	13610	10.0	1693.3	0.00	Stencel	91	34715	2×15.0	4475.7	0.74	Ayres
39	13611	50.0	1693.3	0.00	Stencel	92	34716	2×15.0	4475.8	0.74	Ayres
40	13625	30.0	1695.3	0.01	Stencel	93	34717	2×15.0	4475.8	0.74	Ayres
41	13644	10.0	1697.3	0.03	Stencel	94	34718	2×15.0	4475.9	0.75	Ayres
42	13645	50.0	1697.4	0.03	Stencel	95	34719	2×30.0	4475.9	0.75	Ayres
43	13656	60.0	1699.5	0.05	Stencel	96	35265	2×15.0	4532.5	0.29	Ayres
44	13657	10.0	1699.5	0.05	Stencel	97	35266	2×15.0	4532.5	0.29	Ayres
45	13672	60.0	1701.4	0.07	Basri	98	35269	2×30.0	4532.7	0.29	Ayres
46	13673	10.0	1701.5	0.07	Basri	99	35271	2×14.0	4532.8	0.29	Ayres
47	13691	60.0	1704.5	0.10	Wing	100	35276	2×100.0	4533.3	0.30	Ayres
48	13692	10.0	1704.5	0.10	Wing	101	35277	2×100.0	4533.4	0.30	Ayres
49	13700	30.0	1706.4	0.12	Wing	102	35605	2×30.0	4579.5	0.74	Ayres
50	13721	60.0	1710.4	0.16	Stencel	103	35609	2×30.0	4580.5	0.75	Ayres
51	13722	10.0	1710.4	0.16	Stencel	104	40567	14.5	5268.7	0.37	Rawley
52	13741	60.0	1712.4	0.18	Ayres	105	43992	30.0	5667.5	0.20	Ayres
53	13742	10.0	1712.4	0.18	Ayres	106	44038	30.0	5674.4	0.27	Ayres

analysis of several key features that were not observed by the medium and high resolution gratings of the GHRS.

2. DATA REDUCTION

The fundamental data are 106 large-aperture SWP-HI observations available in the *IUE* archives. These are the same observations discussed in Paper I, although we avoided the 13 small-aperture spectra due to the uncertainties in the absolute flux scale of such data. Table 1 summarizes the SWP-HI exposures, including an identification number that will be used here. Images 89–103 are multiple exposures in the large aperture. The orbital phases were computed using the ephemeris cited by Ayres (1988), where phase 0.0 is the conjunction with the G8 star in front.

Rather than use the standard IUESIPS software to reduce the data, we have implemented a state-of-the-art photometric correction and spectral extraction procedure to eliminate the fixed pattern noise that has long plagued spectra processed with the IUESIPS (see Ayres 1993). Our reduction techniques have to a large extent been described in Paper I, although here we have extended the approach to the full echelle format. In Figure 1, a spectrum processed with our techniques is compared with the same spectrum processed using IUESIPS. The former is noticeably less noisy than the latter, due partly to the successful suppression of the fixed pattern noise, and partly to the "Optimal" extraction procedure.

The flux calibration was based on the DA white dwarf G191-B2B. We also used the white dwarf echellograms as a template

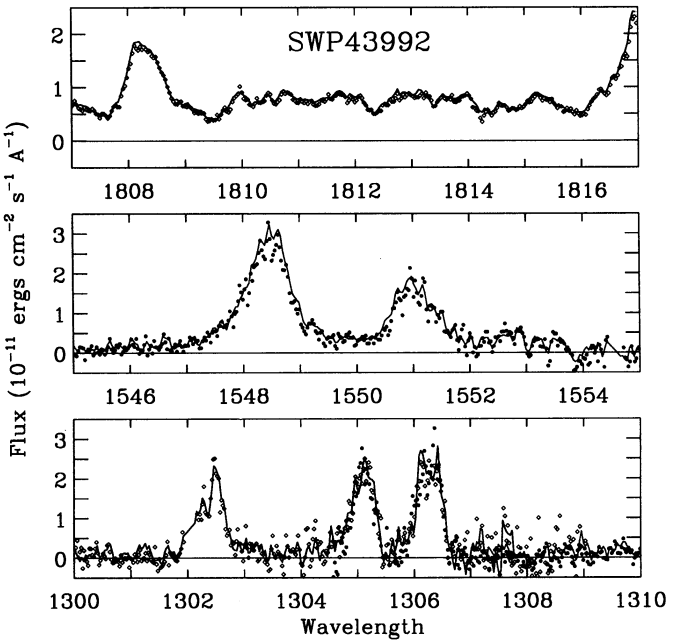

FIG. 1.—Comparison of standard IUESIPS processed spectrum (SWP 43992; *dots*) with our own procedure (*solid curves*). In the lower panel, results from adjacent echelle orders are overplotted for IUESIPS ($m = 106$ [*open diamonds*]; $m = 105$ [*solid dots*]). There is less overlap in our processing: the break point is near 1308 Å. The IUESIPS spectra were smoothed slightly with a $2^{1/2}$ pixel FWHM Gaussian to compensate for the oversampling of the IUESIPS diagonal extraction slit compared with the normal sampling in the rotated reference frame we utilize. Even so, our spectra clearly have less noise than the IUESIPS. Part of the improvement comes from our photometric linearization, which suppresses "fixed pattern" noise. Additional improvement comes from our piecewise "Optimal" extraction procedure (see Paper I).

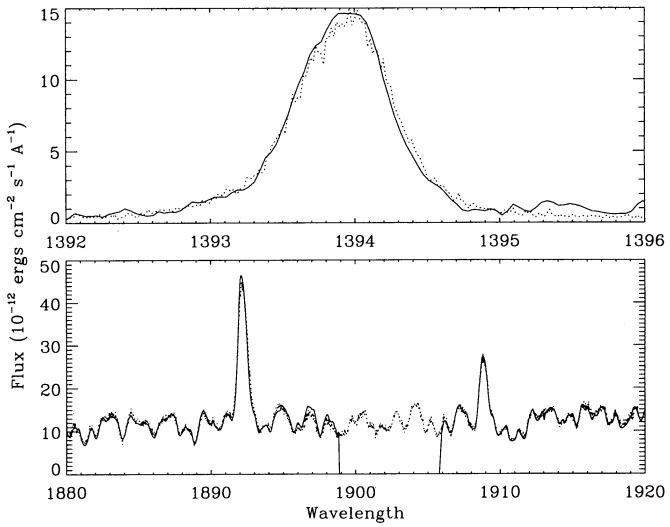

FIG. 2.—A comparison of co-added *IUE* (*solid line*) and GHRS (*dotted line*) spectra. The upper plot compares the Si IV λ1394 line profiles observed by both instruments, and the lower plot shows the 1880–1920 Å spectral region as seen by both the *IUE* and GHRS. The GHRS spectrum in the top (*bottom*) panel is from a single 6.3 (4.5) minute exposure. The *IUE* spectra are based on a co-addition of 31 individual *IUE* spectra representing a total exposure time of 1498 minutes. Note the broad wings of the Si IV line visible in both profiles, particularly the stronger blue wing.

to remove residual order tilts, splays, and small-scale shears, following the initial rotation of the echelle pattern (cf. Paper I). The dispersion relations, including time and temperature corrections were based on an extensive study of the *IUE*'s wavecal lamp. In calibrating the individual spectra, we accounted for the telluric and spacecraft velocities, and compensated for any imposed image shifts indicated by the offset reference point stated in the observing script. We also compensated for the small ($\approx 1''$) systematic shift in the large aperture that arises for bright star acquisitions (underlap mode).

We further increased the accuracy of our fluxes and wavelengths by choosing one of the spectra as a template and cross-correlating the other spectra against it. More precisely, we used several continuum bands in the 1800–1920 Å region for the cross-correlation procedure. The continuum flux should be relatively invariant with time, and the numerous photospheric absorption lines provide many spectral features that are useful in the wavelength cross correlation process (see Fig. 2). Figure 2 compares co-added SWP-HI images of Capella with high-quality GHRS spectra from Paper II.

Figure 3*a* depicts the scale factors that were multiplied by the fluxes in each spectrum to obtain corrected fluxes. These scale factors have been normalized to ensure that the continuum fluxes in the 1880–1920 Å region agree with those observed by the GHRS (see Paper II). The more recent *IUE* spectra have higher correction factors, presumably due to the degradation of the SWP camera's sensitivity with time. This sensitivity degradation has been monitored in low-resolution spectra by observations of standard stars (see Bohlin & Grill-

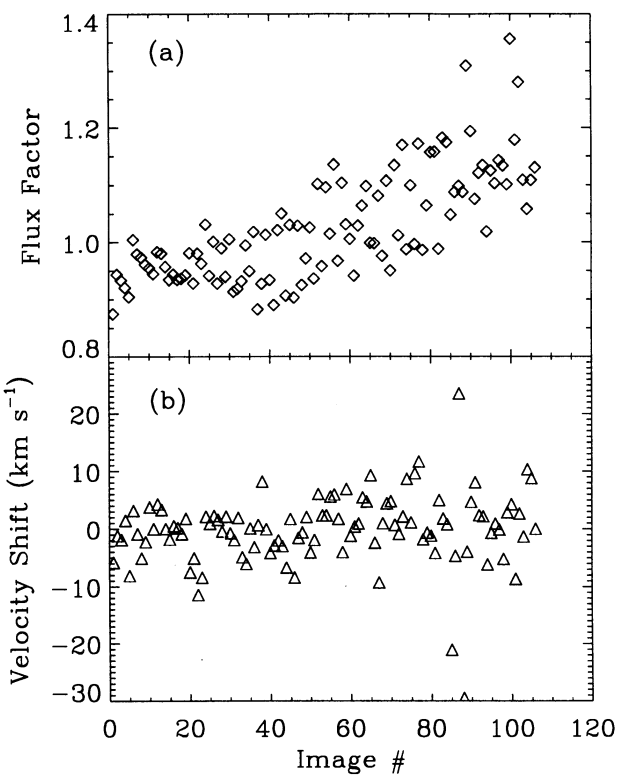

FIG. 3.—(*a*) Ratios of GHRS to *IUE* continuum fluxes that we have used to adjust each *IUE* spectrum to a common flux scale. The 106 spectra are identified using the image numbers listed in Table 1. The increase in flux factor with image number is due to the sensitivity degradation of the SWP camera. (*b*) The velocity shifts applied to the wavelengths in each spectrum to obtain corrected wavelengths. These shifts were computed by cross-correlating the spectra against a templete, with the resulting corrections normalized so that the average shift is 0 km s^{-1}.

mair 1988). It has not been characterized, however, in the echelle mode, so accounting for the degradation is more difficult in high-resolution spectra (see Paper I). That provides additional motivation for our continuum normalization procedure.

Figure 3*b* depicts the velocity shifts that were applied to the wavelengths in each spectrum. These shifts were normalized so that the average would be 0 km s^{-1}. The spectra with ID numbers 85, 86, and 88 are discrepant. There is no obvious reason that these spectra should deviate so wildly, particularly since other spectra obtained close in time appear to be normal.

As one might expect, the continuum features we are using for the cross-correlation closely follow the rest frame of the hotter G1 star. Initially, we assumed that the continuum arose solely in the rest frame of the G1 star. However, after computing all of the velocity shifts, we found a slight dependence of the inferred shift on orbital phase, indicating a small contribution by the G8 star. Based on the photospheric temperatures given in Batten et al. (1991), we would expect the G8 star to account for about 10% of the total continuum flux. When we recomputed the velocity shifts including a 10% contribution from the G8 star, the dependence of velocity shift with orbital phase did indeed disappear. If the three discrepant points in Figure 3*b* are disregarded, the standard deviation of the velocity shifts is 4.6 km s^{-1}, which is comparable to the random error associated with centering a target in the large aperture.

We caution that the flux scale factors and velocity shifts in Figure 3 were applied uniformly to all orders of the SWP-HI echellograms, even though they were determined only from specific continuum bands in the 1800–1920 Å spectral region. Our experience with the wavecal lamp indicates that the systematic shifts of the format are "velocity-like"; thus a wavelength correction determined in one part of the spectrum should be broadly applicable. Whether the same is true for photometric sensitivity variations is more problematic (see below).

3. THE SEARCH FOR LINE PROFILE VARIABILITY

We focused our attention on 18 different emission lines from 12 orders of the echelle pattern. These are listed in Table 2. For all 106 spectra, the complete set of lines was fitted with single Gaussians. We used a semiautomated procedure to do the fitting, but all the resulting fits were verified by eye. Not all of the lines could be accurately measured in all of the spectra. For example, the weaker lines could not be detected in short exposures, and Si II λ1808, Si III] λ1982, and C III] λ1909 are overexposed in deeper observations. For each fit, we determined the line velocity, the full width at half-maximum intensity (FWHM), and the integrated flux of the line. We estimated the uncertainties in these quantities using the procedures outlined by Lenz & Ayres (1992) and the assigned photometic errors determined from our specialized processing. The line fluxes listed in Table 2 are weighted averages of the fluxes measured in the individual spectra. Since the velocities of the lines depend strongly on orbital phase (see Fig. 5), as do the line widths for some lines (see Fig. 6), the velocities and widths in Table 2 were determined using only the observations made at orbital phase $\phi = 0.25 \pm 0.05$. We chose that phase—the quadrature where the G1 star is moving toward the observer and the G8 star is moving away—so we could compare our measurements with those reported in Paper II using GHRS observations, the bulk of which were made at $\phi = 0.26$. As shown in Table 2, most of the GHRS fluxes and velocities agree well with the *IUE* values we have derived, within the cited 1 σ uncertainties. The direct comparison of GHRS and co-added *IUE* spectra made in Figure 2 graphically demonstrates the excellent agreement between the two instruments.

The line widths measured by the *IUE* and GHRS agree fairly well with each other, although for the C IV and Si IV lines the GHRS values are systematically larger by 15%. The systematic enhancement is probably due to the broad wings of these lines which are apparent in the GHRS spectra (see Paper II), but are buried in the noise of the individual *IUE* spectra. By co-adding all the $\phi = 0.25 \pm 0.05$ *IUE* spectra, however, the broad wings—the subject of considerable discussion in Paper II—become apparent in the *IUE* data as well (see Si IV λ1394 in Fig. 2).

The *IUE* values and their uncertainties given in Table 2 are weighted averages and standard deviations of the values measured in the individual spectra. In general, the flux, velocity, and FWHM uncertainties listed in Table 2 are larger than the flux, velocity, and FWHM uncertainties of the individual Gaussian fits. This suggests that if instrumental effects can be ignored, the global standard deviations might actually rep-

TABLE 2

EMISSION-LINE PARAMETERS

	Line		Flux (10^{-12} ergs cm^{-2} s^{-1})		Velocity (km s^{-1})		FWHM (Å)	
ID #	ID	Wavelength	IUE	GHRS	IUE	GHRS	IUE	GHRS
1	N V	1238.821	6.9 ± 1.5	...	38 ± 12	...	0.58 ± 0.07	...
2	N V	1242.804	2.4 ± 0.7	...	24 ± 14	...	0.42 ± 0.12	...
3	S I	1295.653	1.7 ± 0.4	1.81±0.07	22 ± 6	16±1	0.29 ± 0.04	0.33±0.01
4	O I	1304.858	11.3 ± 1.7	11.5±0.5	34 ± 4	29±3	0.47 ± 0.04	0.47±0.02
5	O I	1306.029	13.0 ± 1.9	12.2±0.6	29 ± 4	23±2	0.45 ± 0.04	0.43±0.02
6	C II	1334.532	15.4 ± 2.0	...	24 ± 8	...	0.89 ± 0.10	...
7	C II	1335.708	16.8 ± 1.7	...	44 ± 5	...	0.75 ± 0.05	...
8	Cl I	1351.657	2.0 ± 0.4	...	8 ± 8	...	0.25 ± 0.07	...
9	O I]	1355.598	3.3 ± 0.6	...	24 ± 6	...	0.42 ± 0.05	...
10	Si IV	1393.755	14.3 ± 1.6	12.1±0.3	33 ± 4	35±2	0.73 ± 0.07	0.83±0.02
11	Si IV	1402.770	6.9 ± 1.1	6.9±0.3	31 ± 6	25±3	0.66 ± 0.11	0.81±0.02
12	C IV	1548.202	30.0 ± 2.4	28.6±0.8	24 ± 5	23±3	1.05 ± 0.07	1.19±0.02
13	C IV	1550.774	16.2 ± 1.6	15.9±0.6	28 ± 4	30±3	0.87 ± 0.10	0.96±0.03
14	He II	1640.438	8.2 ± 0.8	7.5±0.5	36 ± 6	37±4	0.67 ± 0.06	0.74±0.03
15	O III]	1666.153	4.2 ± 0.7	3.7±0.1	14 ± 7	21±1	0.60 ± 0.10	0.59±0.01
16	Si II	1808.012	8.0 ± 0.5	...	29 ± 3	...	0.53 ± 0.02	...
17	Si III]	1892.030	23.4 ± 2.1	26.3±0.4	24 ± 3	22±1	0.65 ± 0.03	0.67±0.01
18	C III]	1908.734	10.9 ± 0.8	9.9±0.2	20 ± 3	21±1	0.59 ± 0.03	0.53±0.01

resent true line profile variability. Unfortunately, we believe that instrumental effects do account for much of the variance. One indication is that the line fluxes we measure from spectra with exposure times longer than 30 minutes are generally higher than those we measure from spectra with shorter exposures. This effect, which probably is caused by nonlinearities in the intensity transfer function at low intensities, may be partially responsible for the enhanced sample standard deviations of the line fluxes in Table 2. Despite the possible instrumental effects, we note that the secular standard deviations of the line fluxes typically are only about 10% or less for the strong high-excitation lines that arise primarily from the G1 star.

To specifically search for line profile variations on long timescales, we divided the 106 spectra into four time periods. Using the image ID numbers given in Table 1, the four groups consist of images 1–23, 24–65, 66–88, and 89–106. For each group, the emission-line parameters were determined in the same way as the parameters given in Table 2. The results are shown in Figure 4, where the velocities, FWHM, and fluxes have been normalized to the values given in Table 2. The normalized line parameters of each of the 18 emission lines are labeled using the ID numbers given in Table 2. As was the case in Table 2, the velocities and widths in Figure 4 were calculated only for the $\phi = 0.25 \pm 0.05$ images while the fluxes were calculated using images taken at all orbital phases.

Based on Figure 4, there is no evidence that the emission lines have any collective long-term velocity variations, but there is modest evidence for long-term line flux and line width variability in Capella's emission lines. The line fluxes measured in the most recent time period (*squares*) and the earliest time period (*asterisks*) tend to be lower than those measured in the other two time periods for most of the emission lines. It is possible that this represents intrinsic long term variability. In Paper I, it was noted that Lyα profiles observed during the earliest and latest of our time periods are different from those observed during the intervening periods. Therefore, the flux variability indicated in Figure 4 might conceivably be connected with the Lyα variability discussed in Paper I.

However, there are two reasons to be cautious concerning the apparent long term flux variability implied by Figure 4. First, most of the images made in the earliest time period (images 1–23) have short exposure times of 30 minutes or less. Therefore, the fluxes might be expected to be lower than average, based on the correlation between flux and exposure time noted earlier. Second, the fluxes measured during the most recent period are lower than normal for almost all of the emission lines, but the effect is obviously more pronounced for lines with shorter wavelengths (smaller line ID numbers). That behavior suggests an instrumental effect and is almost certainly due to stronger sensitivity degradation for shorter wavelengths; an effect that Bohlin & Grillmair (1988) observed in low-resolution spectra. Our attempt to correct for the sensitivity degradation was made using a continuum region in the long-wavelength region of the SWP camera, which explains why the fluxes measured in different time periods agree better for the lines with longer wavelengths (larger line ID numbers). We may have successfully corrected for the sensitivity degradation of the SWP camera for lines 9–18, but this is clearly not the case for lines 1–8. Consequently, the flux uncertainties given in Table 2 for lines 1–8 might be almost entirely an effect of the sensitivity degradation.

The line widths in Figure 4 seem to imply that the emission lines observed during the third time period (*triangles*) are broader than average and those observed during the last time period (*squares*) are narrower than average. We checked the validity of the apparent long-term changes in FWHM by checking the observations made at orbital phase $\phi = 0.75 \pm 0.05$ for the same types of changes. In the $\phi = 0.75 \pm 0.05$ observations, there is no evidence that the emission lines were broader than normal during the third time period or that they were narrower than normal during the most recent period. Thus, there is no strong evidence for long-term variations in line widths, since any such variation should not be dependent on orbital phase. One could imagine that profile variations might be dependent on the rotation phase of the G1 star that dominates Capella's UV line emission, but the G1 star's rotation period is much shorter than Capella's orbital period.

We conclude that we have no compelling evidence for intrinsic long term line profile variations, except for those in the Lyα line noted in Paper I. When the systematic effects discussed above are taken into account, we believe that our data indicate intrinsic line flux and line width variations of only about 5% or less, and line velocity variations of only a few kilometers per second at most.

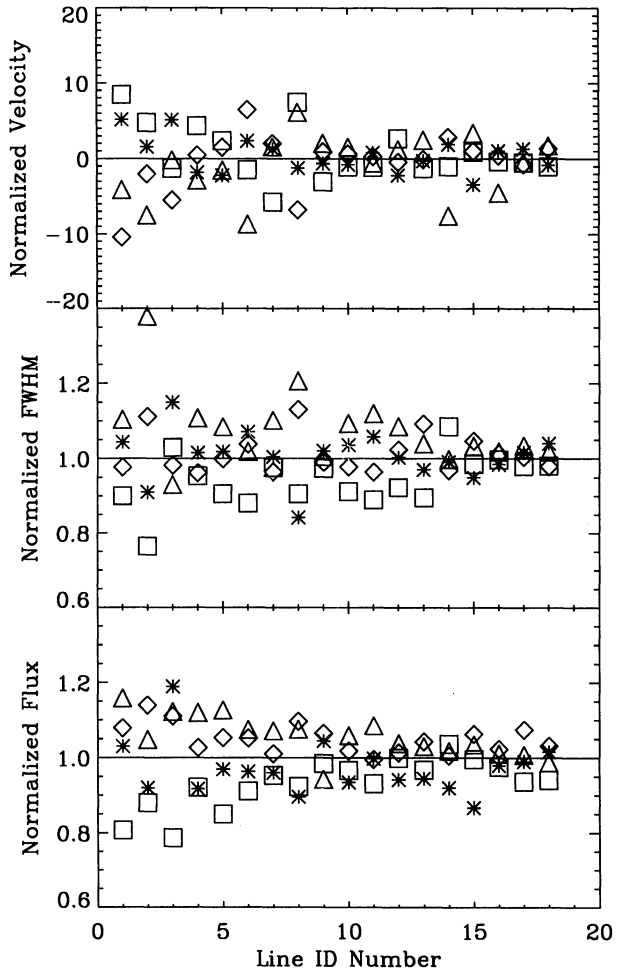

FIG. 4.—We divided the 106 *IUE* spectra into four time periods: images 1–23 (*asterisks*), 24–65 (*diamonds*), 66–88 (*triangles*), and 89–106 (*squares*). For each group we have computed average line profile parameters for the 18 lines listed in Table 2 and normalized them to the values in Table 2.

This lack of variability is remarkable considering the existence of significant variability on many other stars, both active and inactive (see Ayres et al. 1995, and references therein). In particular, hyperactive RS CVn binaries can show large UV line flux variations on timescales of hours, days, and weeks. The Sun, a relatively inactive star, shows significant ($\approx$30%) UV emission line variations associated with both its rotational cycle and its 11 yr activity cycle (Rottman et al. 1982; Mount & Rottman 1981).

For Capella, the lack of UV emission line variability suggests that the surface of Capella's G1 star must be uniformly covered by small-scale active regions that individually might be highly variable, but collectively are not. This is in contrast to the Sun and the RS CVn stars, whose surfaces are dominated by a few large active regions. The magnetic field structures on the Capella G1 star might instead have many similarities with the magnetic supergranulation network on the Sun, which is pervasive on the solar surface and is relatively unaffected by the solar activity cycle. In Paper II, it was proposed that a large fraction of the G1 star's transition region line emission might be from stellar analogs of solar transition region explosive events (Dere, Bartoe, & Brueckner 1989). Since these explosive events uniformly cover the surface of the Sun, the possible existence of similar phenomena on the G1 star is consistent with Capella's lack of variability. Perhaps the fundamental cause of Capella's lack of variability is the G1 star's relatively shallow convective envelope. The shallow convection zone might be capable of producing and amplifying significant small-scale magnetic fields, but not the large flux ropes of solar-like active regions.

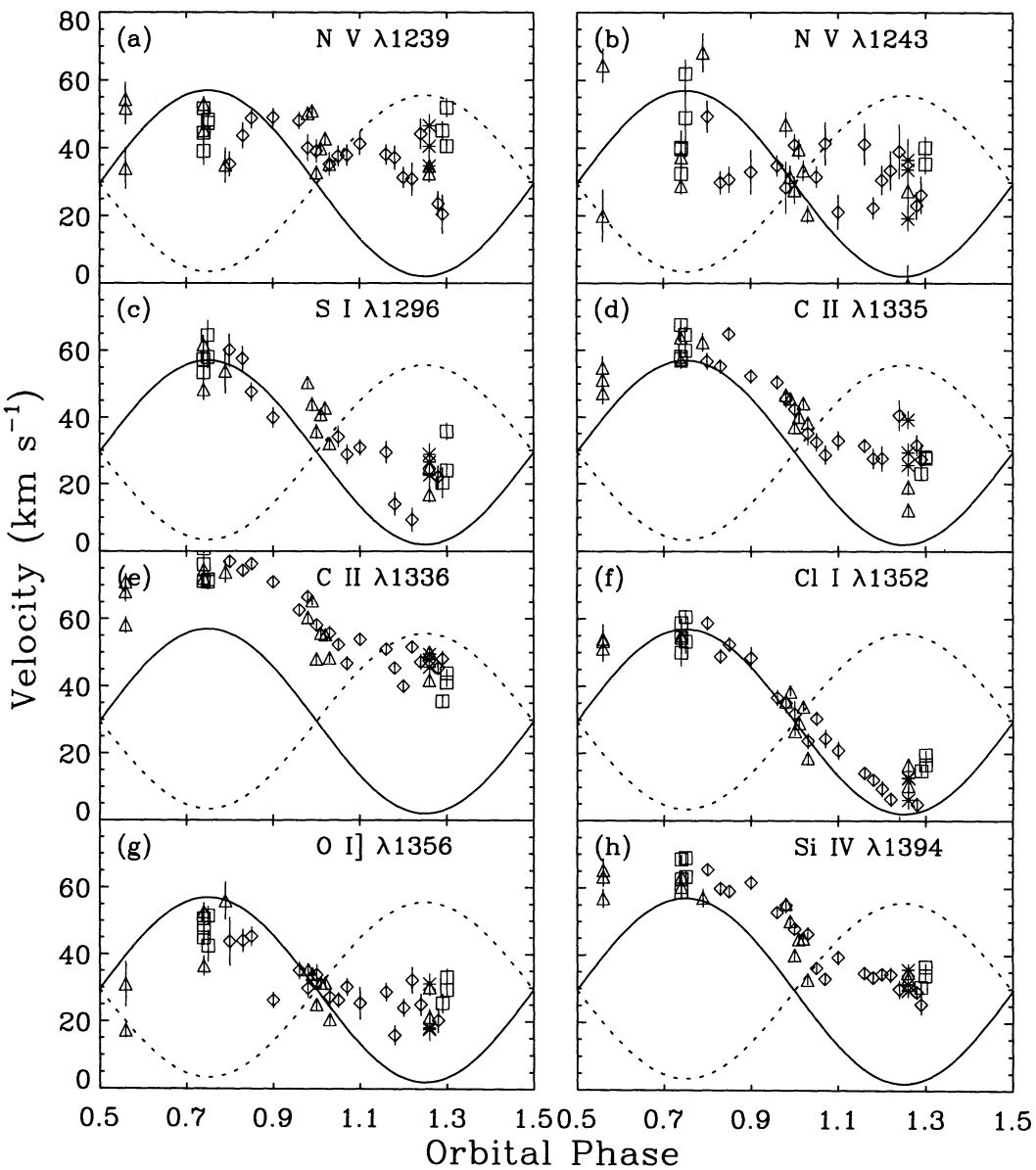

FIG. 5.—Plots of line velocities as a function of orbital phase for 14 different emission lines. The symbols have the same meaning as in Fig. 4. Solid lines represent the rest frame of the G1 star, and dotted lines represent the rest frame of the G8 star. Measurements made on spectra with exposure times of 30 minutes or less were omitted for clarity (except for Si III] λ1892 and C III] λ1909).

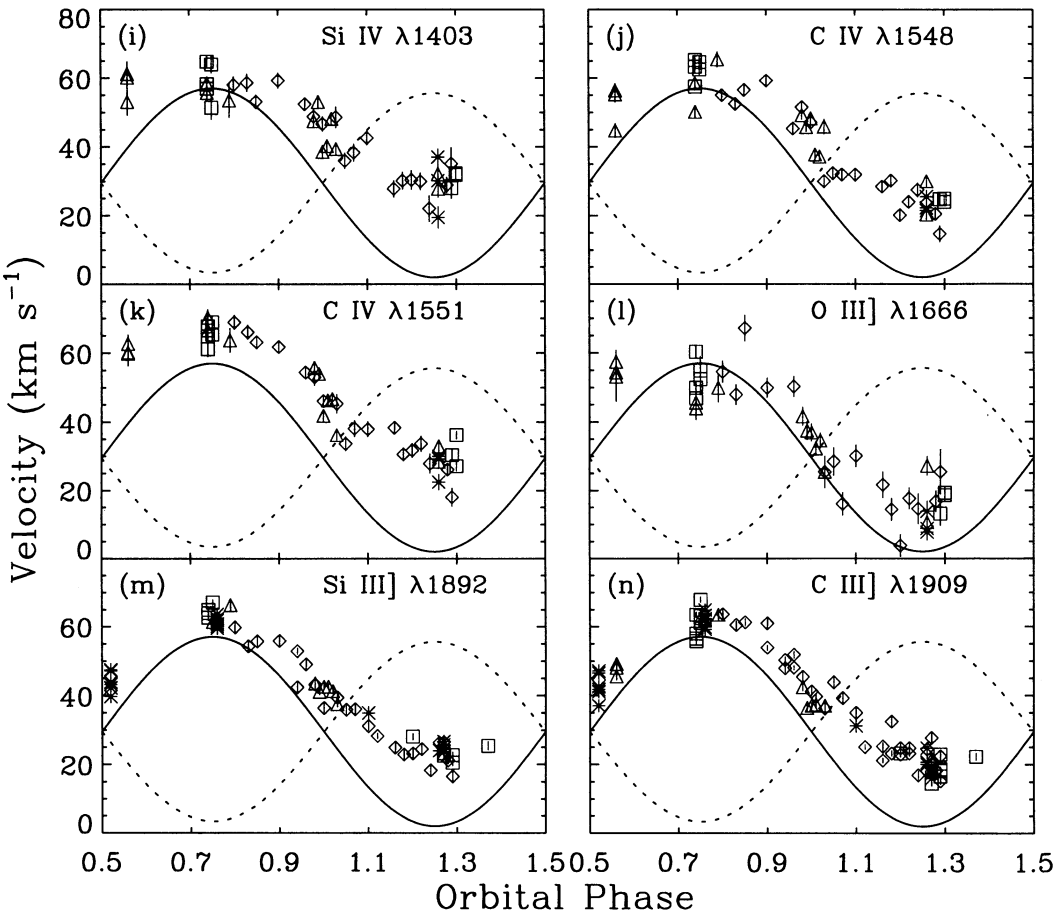

FIG. 5—*Continued*

4. INFERRING THE CONTRIBUTIONS OF THE G1 AND G8 STARS TO CAPELLA'S EMISSION LINES

The velocities we measure in the individual spectra are shown explicitly in Figures 5 and 6, indicating the variation with orbital phase. For purposes of clarity, the measurements from exposures of 30 minutes or less are not shown, with the exception of the Si III] λ1892 and C III] λ1909 lines for which the deeper integrations are overexposed. The solid lines in Figures 5 and 6 indicate the rest frame of the G1 star, and the dotted lines indicate the rest frame of the G8 star. In general, the line velocities tend to follow the velocity of the G1 star more closely than the G8 star, implying that the G1 star is responsible for most of the line emission. For some lines, however, the G8 star's contribution is significant enough to cause noticeable broadening of the lines at quadrature, where the difference in radial velocity between the G1 and G8 stars reaches a maximum. The dependence of line width on orbital phase is shown in Figure 6, jointly with the velocity dependence, for the four lines in which the width dependence is most obvious.

The dependence of velocity and/or FWHM on orbital phase is a key source of information about the relative contributions of the G1 and G8 stars to Capella's emission lines. We have conducted numerical experiments to simulate how Capella's line velocities and line widths measured by single Gaussian fits would vary with orbital phase, assuming various characteristics for the emission from the G1 and G8 stars. Figure 7 depicts the results from one such simulation. In all of the simulations we assumed that the emission profiles of the G1 and G8 stars are Gaussian. For the simulation used to produce Figure 7, we assumed that the emission profile of the G1 star has a line width of FWHM = 0.7 Å and that of the G8 star, FWHM = 0.4 Å; comparable to values estimated in Paper II in the multi-Gaussian dissection of the GHRS transition region line profiles. We also assumed that the G1 star's emission was redshifted by 15 km s^{-1} with respect to the rest frame of the G1 star, and that the G8 star's emission was redshifted by 5 km s^{-1} with respect to the rest frame of the G8 star. Finally, we ran the simulation for seven different flux ratios for the G1 and G8 star components.

The data in Figures 5 and 6 can be compared with Figure 7 to obtain a rough estimate of the flux contributions of the G1 and G8 stars to the emission lines. When the fluxes from the G1 and G8 stars are the same, the velocity measured by the single-Gaussian fit tends to follow the narrower G8 star emission. As the ratio of the fluxes from the two stars rises above 1.5, however, the velocity begins to follow the G1 star more closely. As one would expect, the line is broadest at quadrature, where the velocity separation between the G1 and G8 star components is largest. Since the G1 star emission was assumed to be redshifted by 10 km s^{-1} more than the G8 star emission, the velocity separation at the $\phi = 0.75$ quadrature is greater than the velocity separation at the $\phi = 0.25$ quadrature; thus the line width at $\phi = 0.75$ is greater than at $\phi = 0.25$. Consequently, a difference in line widths at $\phi = 0.25$ and $\phi = 0.75$,

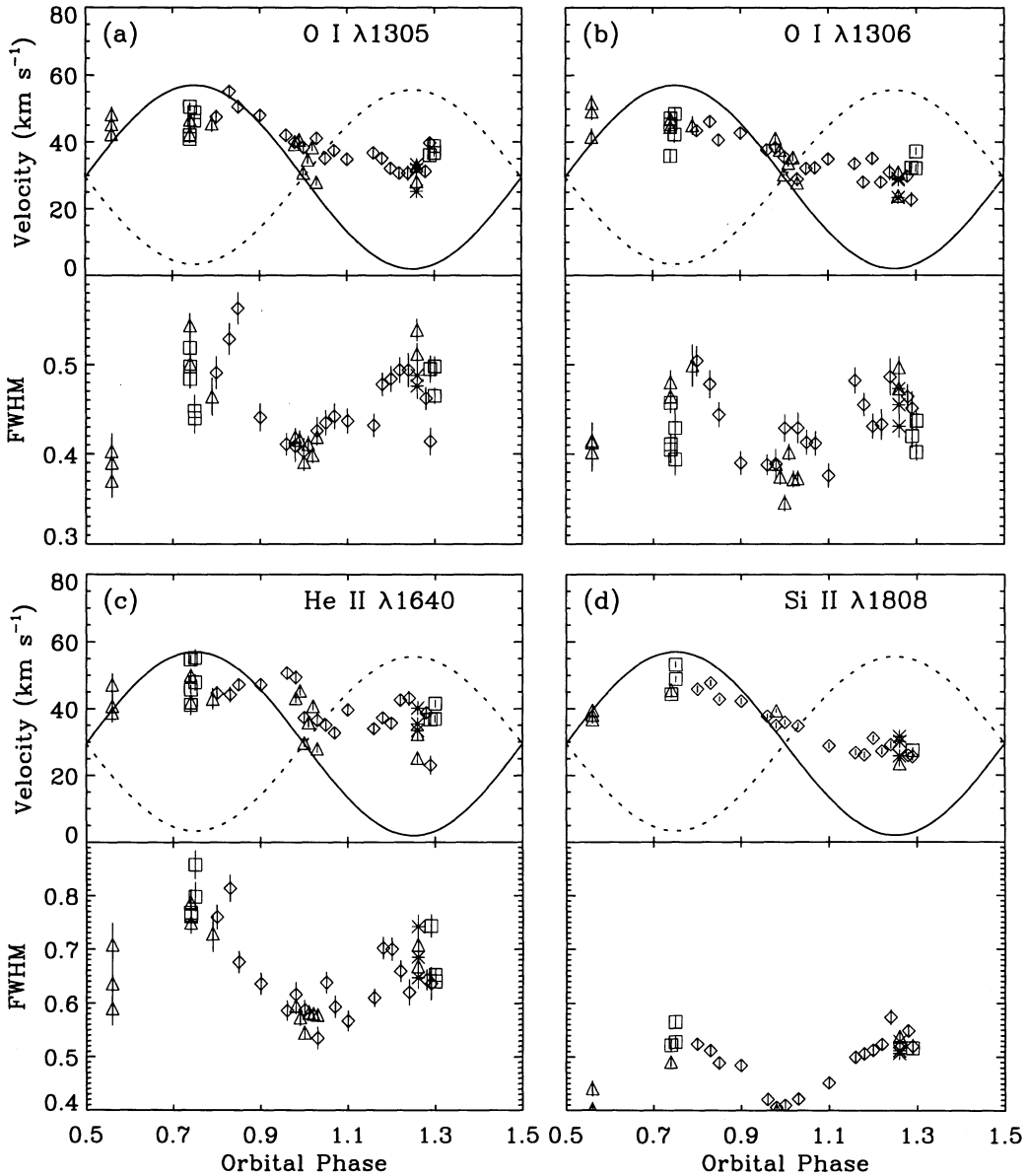

FIG. 6.—Plots of line velocities and line widths as a function of orbital phase for four different emission lines. The symbols have the same meaning as in Fig. 4. Solid lines represent the rest frame of the G1 star, and dotted lines represent the rest frame of the G8 star. Measurements made on spectra with exposure times of 30 minutes or less were omitted for clarity.

such as that seen for He II (see Fig. 6*c* and § 5.3), can be used to infer a difference in line redshifts for the G1 and G8 star components.

5. A DISCUSSION OF INDIVIDUAL LINES

5.1. N V λλ1239, 1243

With the exception of the S I λ1296, Cl I λ1352, and O I] λ1356 lines, all the features in Figure 5 are transition region lines. The velocities generally follow the G1 star quite well, suggesting that the G8 star is responsible for only a small fraction of the transition region line emission (e.g., Ayres 1988). This does not seem to be the case for the two N V lines, however. In Paper II, it was suggested, on the basis of multi-Gaussian modeling, that the G8 star is responsible for about 30% of Capella's N V flux. Figures 5*a* and 5*b* show a lack of velocity dependence on orbital phase which supports that conclusion. As discussed in Paper II, the prominence of the G8 star in the N V lines is probably due to "evolved" abundances. Since the G8 star is in the postflash "clump" phase, nitrogen-rich material processed by the CNO cycle very likely was dredged up from its interior during the first ascent of the giant branch.

5.2. S I λ1296, Cl I λ1352, *and* O I] λ1356

Unlike the transition region lines, the G8 star has generally been found to be a more significant contributor to chromospheric lines, such as Lyα (Linsky et al. 1993), Mg II λλ2796, 2803 (Ayres 1988; Paper II), Si II λ1808 (Ayres 1988), and the O I triplet near 1300 Å (Ayres 1988; Paper II). Figures 6*a*, 6*b*, and 6*d* also suggest that the G8 star is a strong contributor to

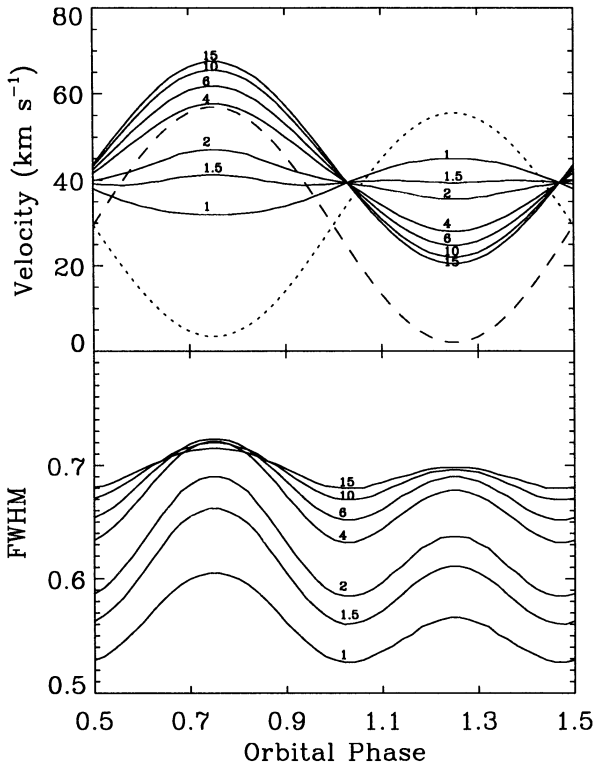

FIG. 7.—A simulation of how emission-line velocities and widths, as measured by single Gaussian fits, change with orbital phase assuming seven different values of the G1/G8 flux ratio (numerical entries in figure). We assumed that the emission lines of the G1 and G8 stars have widths of 0.7 Å and 0.4 Å, respectively. We also assumed a line redshift of 15 km s^{-1} for the G1 star and 5 km s^{-1} for the G8 star emission. The dashed line represents the rest frame of the G1 star, and the dotted line represents the rest frame of the G8 star.

the O I and Si II lines. However, the G8 star apparently is not a strong contributor to three of the chromospheric lines we have considered, namely S I λ1296, Cl I λ1352, and O I] λ1356 (see Figs. 5*c*, 5*f*, and 5*g*).

The G1 star is not quite as dominant in the O I] λ1356 line as it is in the S I and Cl I lines, but it is clearly more dominant in the O I] intersystem line than it is in the O I resonance lines (see Figs. 6*a* and 6*b*). In Paper II, it was noted that for the chromospheric lines the G8 star's flux contribution seemed to depend on the opacity of the line, with the G8 star's contribution being larger in the more optically thick lines. Our measurements of the O I] line are consistent with such a correlation. Such a correlation might arise if the chromospheric emission from the G1 star is much more optically thick than that of the G8 star. If this is the case, the emission from the G1 star could be suppressed somewhat by "effective thickness" in the thickest lines, resulting in the G8 star's being responsible for a larger fraction of the observed flux in such lines.

We believe that a different phenomenon produces the dominance of the G1 star in the S I and Cl I lines. In his analysis of solar spectra, Shine (1983) found that the Cl I λ1352 line is radiatively pumped by the C II λ1336 line. Ayres (1988), who previously noted the G1 star dominance in the Cl I line, suggested that the fluorescence mechanism also is operating on Capella. Since the C II λ1336 line is a transition region line that is clearly dominated by the G1 star (see Fig. 5*e*), the Cl I λ1352 line excited by this C II line should also be dominated by the G1 star.

Like the Cl I λ1352 line, the S I λ1296 line is radiatively excited by a strong emission line. The S I line, in fact, is pumped by both the O I λ1302 and O I λ1306 lines (Brown & Jordan 1980). Because the two O I resonance lines are chromospheric features for which the G8 star is a significant contributor, it is not immediately apparent why the fluoresced S I line would be dominated by the G1 star. In Paper II, all three O I resonance lines were subjected to multi-Gaussian modeling. The O I features from the G1 star and the G8 star were found to have average widths of FWHM = 0.50 Å and 0.21 Å, respectively. The O I emission line profiles from both stars are shown schematically in Figure 8, which also indicates the location of the radiatively pumped S I 1305.89 Å and 1302.34 Å lines relative to the O I lines. Both S I lines lie in the *wings* of the narrow G8 star line, but they are on the *shoulders* of the broader G1 star line profile. Therefore, we believe that the fluorescence mechanism producing the S I λ1296 line is much stronger on the G1 star than on the G8 star simply because the G1 star's O I lines are broader. A consequence of this is that the G1 star's O I emission must be broad *in the rest frame of the star*, and not be apparently broad simply due to the influence of fast stellar rotation.

5.3. He II λ1640

Most of the transition region lines observed from Capella are found to be significantly redshifted, as shown in Figure 5. Transition region line redshifts are seen for many other stars as well, and the usual explanation is that the emissions are produced in the downward leg of a circulation system (Ayres, Jensen, & Engvold 1988). Unlike the transition region lines, chromospheric lines are generally not found to have large redshifts. The He II λ1640 emission line is different from most features in that it can be either a chromospheric or a transition

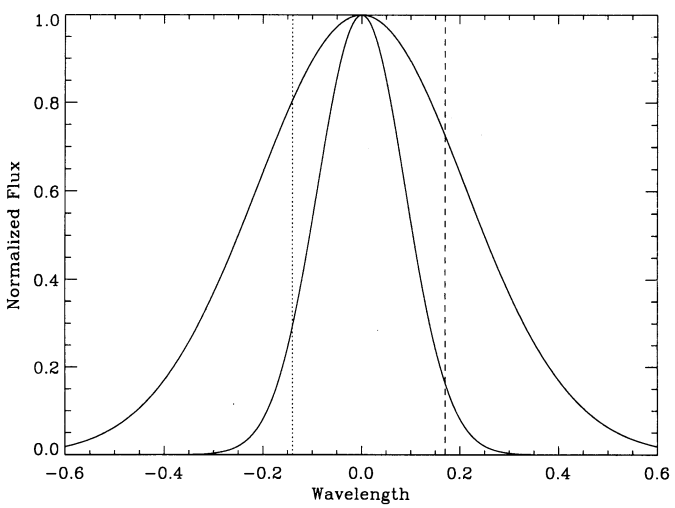

FIG. 8.—The O I emission-line profiles of the G1 and G8 stars are shown schematically; the broader Gaussian represents the G1 star. If the two Gaussians represent O I λ1306, the dotted line marks the location of the pumped S I 1305.89 Å line, which in turn excites the S I λ1296 line. If the two Gaussians represent O I λ1302, the dashed line marks the location of the pumped S I 1302.34 Å line. Both of the pumped S I lines lie out in the wings of the narrow G8 star profile, but they are relatively close to line center in the broader G1 star profile, implying that the fluorescence efficiency might be much higher on the G1 star than on the G8 star.

region line. In the collisional excitation model discussed by Jordan (1975), the He II line is a transition region line formed at a temperature of roughly 10^5 K. In the radiative recombination model, the He II line is a chromospheric line formed at a temperature of roughly 10^4 K (Zirin 1975).

Since transition region lines often have large redshifts and chromospheric lines do not, the velocity observed for the He II line might possibly be used to distinguish whether the emission is formed in the transition region or in the chromosphere (e.g., Athay 1988). In Paper II, it was suggested that the He II emission of the G1 star is from the transition region, but the emission from the G8 star is chromospheric. Figure 6*c* supports that interpretation. The He II line is significantly broader at orbital phase 0.75 than it is at orbital phase 0.25, suggesting that the emission from the G1 star is redshifted more than the emission from the G8 star. In fact, simulations similar to those that produced Figure 7 indicate that the emission from the G1 star is redshifted more than the emission from the G8 star by about 20 km s^{-1}.

In the radiative recombination model, ionizing radiation from the corona is ultimately responsible for the He II emission. In this regard, it is worth noting that while the transition region emissions of the G1 star are strongly enhanced over those of the G8 star, the X-ray fluxes of the two stars might be nearly equal (Ayres et al. 1995). If that is the case, it is natural to expect that the percentage of He II emission arising from radiative recombination would be larger on the G8 star than on the G1 star.

5.4. *The Transition Region Intersystem Lines*

Ayres (1988) estimated that the G1 star accounted for at least 90% of Capella's Si III] λ1892 emission and at least 75% of Capella's C III] λ1909 emission. Figures 5*m* and 5*n* suggest that the G1 star is responsible for at least 90% of the emission in both the Si III] and C III] lines. Figure 5*l* demonstrates a similar G1 star dominance for the O III] λ1666 line.

5.5. C II $\lambda\lambda$1335, 1336

In Figure 9 we present a five-Gaussian fit to the two C II lines. To produce the fit, we first obtained C II profiles at three different orbital phases ($\phi = 0.25 \pm 0.05$, $\phi = 1.00 \pm 0.02$, and $\phi = 0.75 \pm 0.05$) by co-adding all the relevant spectra at those phases. A reseaux mark contaminates the C II λ1335 line, but its effect is mitigated by co-adding spectra in which the defect appears at different apparent velocities owing to different aperture offsets or telluric shifts. Both C II lines show absorption features near line center. The position of the C II λ1335 absorption feature is the same at all three orbital phases, indicating that it must be predominantly interstellar. We thus removed it to produce the profiles shown in Figure 9.

The position of the C II λ1336 absorption feature clearly follows the G1 star with changing orbital phase, so we believe that it is a central reversal in the G1 star's C II λ1336 emission. We cannot rule out the possibility that the C II λ1335 line also has a small central reversal which we failed to detect due to the contaminating interstellar absorption feature. The C II λ1335 line was modeled with two Gaussians—the larger one representing the G1 star, and the smaller one, the G8 star. The C II λ1336 line was modeled similarly, but with an absorption Gaussian added to the G1 star profile to account for the central reversal. We fit the three spectra in Figure 9 simultaneously, assuming that the absorption Gaussian followed the G1 star in velocity.

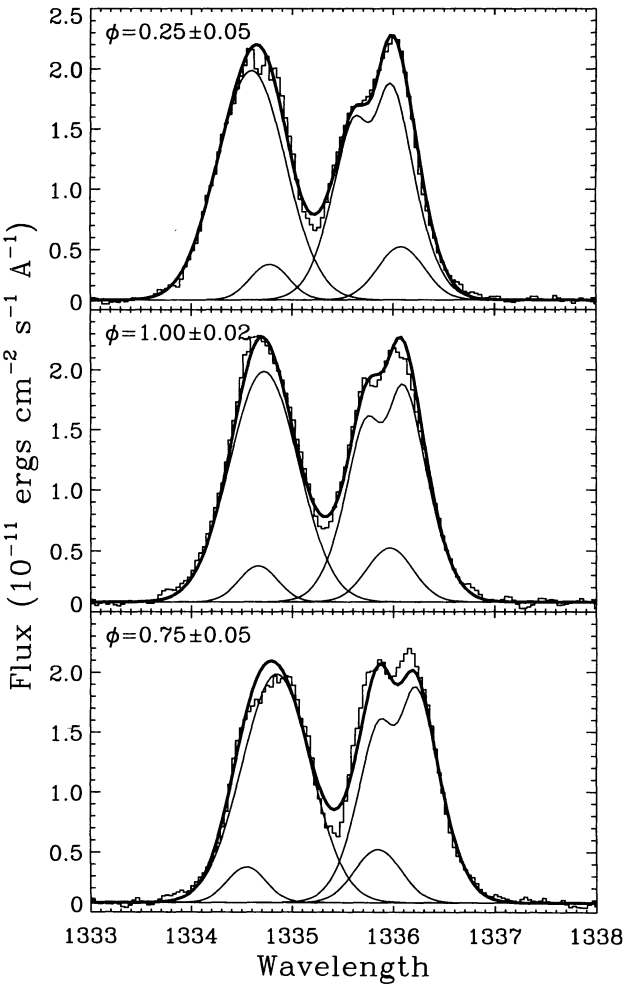

FIG. 9.—The C II profiles at three different orbital phases obtained by co-adding all *IUE* spectra at those orbital phases. The interstellar absorption feature in the C II λ1335 line has been removed. We have fitted the C II lines with five Gaussians; the two largest representing the C II emissions of the G1 star, the two smallest representing the C II emissions of the G8 star, and an absorption Gaussian representing the central reversal of the G1 star's C II λ1336 line.

The parameters of the fit are given in Table 3. The ratio of the G1 star's flux to the G8 star's flux is 11.5 for the C II λ1335 line and 6.1 for the C II λ1336 line, but the errors in the ratios are high. The average of the two values, 8.8, probably is closer to the true flux ratio. The velocities listed in Table 3 indicate that for both stars, the C II λ1336 line is more redshifted than the C II λ1335 line. We believe that the velocity difference is real, but for the G8 star the difference is probably not as high as the fit parameters suggest. This is because the G8 star is only a small contributor to the C II lines, which means that the uncertainties in the G8 star's C II line velocities are very high.

The most interesting property of the fit, however, concerns the central reversal in the C II λ1336 line, which is blueshifted by about 9 km s^{-1} with respect to the emission from the G1 star. Solar C II lines are found to have central reversals, with the C II λ1336 central reversal being somewhat more prominent than that of C II λ1335; the solar C II central reversals are also found to be blueshifted by a few kilometers per second (Lites, Shine, & Chipman 1978). Since the G1 star's C II lines are redshifted, it is possible that the blueshifted central

TABLE 3

MULTIPLE GAUSSIAN FIT TO THE C II LINES

Ion	λ_{rest} (Å)	v^a_{G1} (km s^{-1})	f_{G1} (10^{-12})	$FWHM_{G1}$ (Å)	v^b_{G8} (km s^{-1})	f_{G8} (10^{-12})	$FWHM_{G8}$ (Å)
C II	1334.532	13	16.1	0.80			
C II	1334.532				0	1.4	0.45
C II	1335.708	24	17.6	0.73			
C II	1335.708	15	2.3	0.28			
C II	1335.708				28	2.5	0.54

[a] Velocity with respect to radial velocity of the G1 star.
[b] Velocity with respect to radial velocity of the G8 star.

reversals are due to optically thick accelerating downflows which produce preferential absorption on the blue sides of the emission lines. The blueshifted central reversals might also be explained by proposing that the C II emission from the G1 star consists of two components—an optically thick component with a central reversal and a less optically thick component with a higher redshift. Whatever the interpretation, it is curious that the central reversal of the Si III λ1207 line discussed in Paper II is not blueshifted like that of C II λ1336. Since the Si III λ1207 and C II lines should be formed at similar temperatures, one might expect these lines to behave in a similar fashion. However, the opacity of the C II lines might be much higher than the Si III feature, owing to the larger abundance of carbon and the photoionization of chromospheric neutral carbon by Lyα radiation from the transition region (Lites, Shine, & Chapman 1978).

5.6. Si IV $\lambda\lambda$1394, 1403 *and* C IV $\lambda\lambda$1548, 1551

In Paper II, the multi-Gaussian modeling of the Si IV and C IV lines suggests that the G1 star is more dominant in the C IV lines than it is in the Si IV lines. Figures 5*h*–5*k* provide some support for this assertion, as the C IV line velocities appear to follow the G1 star slightly better than the Si IV line velocities. We believe that this is further evidence that the G8 star's composition is evolved, since material dredged up from the stellar interior should be somewhat depleted in carbon (Lambert & Ries 1981), as well as being nitrogen rich (as discussed in § 5.1).

6. SUMMARY

We have used the extensive set of SWP-HI *IUE* observations of Capella to search for line profile variability, like that seen in H I Lyα in Paper I. We have failed, however, to find evidence for any significant variability. The UV emission line regions on Capella's G1 star must therefore uniformly cover the stellar surface, suggesting that the regions are dominated by small-scale magnetic fields, such as those of the solar network, rather than large-scale magnetic fields associated with large active regions, like those that exist on the Sun and many other stars.

Our study has found encouragingly good agreement between *IUE* and *HST*/GHRS spectra. This not only is comforting for those who have analyzed *IUE* data in the past but also is encouraging for future users of the vast *IUE* archives. In this paper, we have used the *IUE* data to confirm some of the findings of Paper II, which was based on a few GHRS "snapshots" of Capella. In particular, the *IUE* data support the conclusion of Paper II that the G8 star is a surprisingly large contributor to the N V $\lambda\lambda$1239, 1242 lines, probably because of evolved abundances. The *IUE* data also support the claim made in Paper II that the He II λ1640 emission from the G8 star is mostly chromospheric emission excited by ionizing radiation from higher atmospheric layers, while the He II λ1640 emission from the G1 star is mostly collisionally excited radiation from the transition region.

We also have analyzed additional emission lines not covered by the GHRS spectra discussed in Paper II. Unlike most of Capella's chromospheric emission features, we find that the G8 star is not a significant contributor to the S I λ1296, Cl I λ1352, and O I] λ1356 lines. For O I] λ1356, the lack of emission from the G8 star might simply be part of a general trend noted in Paper II for the G1 star to be more dominant in the less optically thick chromospheric lines. We believe the Cl I λ1352 line, however, is dominated by the G1 star because it is radiatively pumped by the C II λ1336 line, which like most of the other transition region lines is dominated by the G1 star. Therefore, the Cl I line is analogous to the He II λ1640 line of the G8 star in that it is excited by radiation from nonlocal regions of the atmosphere. In contrast, we believe that the fluorescence mechanism which produces the S I λ1296 line is simply more efficient on the G1 star than on the G8 star, because the O I resonance lines responsible for the pumping are broader on the G1 star.

Finally, our analysis of the C II $\lambda\lambda$1335, 1336 lines has revealed a blueshifted central reversal in the λ1336 line, similar to central reversals observed in solar C II lines but different from the central reversal of the Si III λ1207 line discussed in Paper II, which is not blueshifted. The apparent difference between the strong C II and Si III lines might be a signature of material circulation systems in the high-chromosphere/low–transition region of the G1 star, and should be the focus of future work, both on Capella itself and on other active Hertzsprung gap giants.

This work is supported by NASA grant S-56500-D to the National Institute of Standards and Technology, and NASA grants NAG 5-1215 and NAG 5-199 to the University of Colorado.

REFERENCES

Athay, R. G. 1988, ApJ, 329, 482
Ayres, T. R. 1984, ApJ, 284, 784
———. 1988, ApJ, 331, 467
———. 1993, PASP, 105, 538
Ayres, T. R., Brown, A., Gayley, K. G., & Linsky, J. L. 1993, ApJ, 402, 710 (Paper I)
Ayres, T. R., Jensen, E., & Engvold, O. 1988, ApJS, 66, 51
Ayres, T. R., & Linsky, J. L. 1980, ApJ, 241, 279
Ayres, T. R., et al. 1995, ApJS, 96, 223
Batten, A. H., Hill, G., & Lu, W. 1991, PASP, 103, 623
Bohlin, R. C., & Grillmair, C. J. 1988, ApJS, 66, 209
Brown, A., & Jordan, C. 1980, MNRAS, 191, 37P

Dere, K. P., Bartoe, J-D. F., & Brueckner, G. E. 1989, Sol. Phys., 123, 41
Dupree, A. K. 1975, ApJ, 200, L27
Dupree, A. K., Brickhouse, N. S., Doschek, G. A., Green, J. C., & Raymond, J. C. 1993, ApJ, 418, L41
Hummel, C. A., Armstrong, J. T., Quirrenbach, A., Buscher, D. F., Mozurkewich, D., Elias, N. M., II, & Wilson, R. E. 1994, AJ, 107, 1859
Jordan, C. 1975, MNRAS, 170, 429
Lambert, D. L., & Ries, L. M. 1981, ApJ, 248, 228
Lemen, J. R., Mewe, R., Schrijver, C. J., & Fludra, A. 1989, ApJ, 341, 474
Lenz, D. D., & Ayres, T. R. 1992, PASP, 104, 1104
Linsky, J. L., et al. 1993, ApJ, 402, 694
Linsky, J. L., Wood, B. E., Brown, A., Andrulis, C., Judge, P., & Ayres, T. R. 1995, ApJ, 442, 381 (Paper II)
Lites, B. W., Shine, R. A., & Chipman, E. G. 1978, ApJ, 222, 333
Mount, G. H., & Rottman, G. J. 1981, J. Geophys. Res., 86, 9193
Pallavicini, R., Golub, L., Rosner, R., Vaiana, G. S., Ayres, T., & Linsky, J. L. 1981, ApJ, 248, 279
Rottman, G. J., et al. 1982, Geophys. Res. Lett., 9, 587
Shine, R. A. 1983, ApJ, 266, 882
Skumanich, A. 1972, ApJ, 171, 565
Strassmeier, K. G., & Fekel, F. C. 1990, A&A, 230, 389
Wood, B. E., Brown, A., Linsky, J. L., Kellett, B. J., Bromage, G. E., Hodgkin, S. T., & Pye, J. P. 1994, ApJS, 93, 287
Zirin, H. 1975, ApJ, 199, L63